EDGE ARTICLE

Check for updates

Nitric oxide-activatable NIR-II organic small molecule for fluorescence imaging-guided synergistic photodynamic and photothermal therapy†

Xinyi Zhang, Ling Li, Yuxin Ren, Meiqi Li, Xinyi Ma, Yajie Long, Junqing Wang and Yanli Tang [ID] *

Precise cancer diagnosis and treatment are vital for reducing mortality. The development of activatable second near-infrared window (NIR-II) imaging-guided tumor phototherapy strategies with excellent tumor specificity and antitumor effects remains a major challenge. In this work, we design and synthesize a D−π−A−π−D organic small molecule CTBA that can be effectively activated by nitric oxide. CTBA exhibits absorption and emission in the visible region. Interestingly, after reacting with excess nitric oxide in the tumor microenvironment, the probe can be converted into CTBT with a new structure, which exhibits excellent NIR-II fluorescence, and photodynamic and photothermal properties under 808 nm excitation. Notably, this activatable probe pioneers the convergence of three critical features: (1) NIR-II imaging capacity for deep-tissue visualization, (2) on-demand therapeutic activation, and (3) synergistic photodynamic−photothermal effects, marking the first report of such an integrated system. By virtue of its "turn-on" property, this probe significantly reduces the background noise of imaging and the damage to normal tissues during phototherapy. Then, CTBA-NPs are constructed by self-assembly between CTBA and PS_{1000}−PEG_{2000}, which can achieve highly accurate and efficient tumor diagnosis and treatment *in vitro* and *in vivo*. This work provides a promising strategy for designing activatable multifunctional NIR-II fluorescent probes for precise theranostics.

Introduction

Cancer is one of the major diseases that threaten public health. Early diagnosis and precise treatment of cancer are the key to reducing mortality.[1–6] Fluorescence diagnosis and phototherapy can simultaneously perform light-induced cancer diagnosis and treatment with the characteristics of non-invasiveness, low drug resistance, and real-time monitoring.[7,8] Compared with visible light (400–700 nm) and NIR-I (700–900 nm) windows, the NIR-II (>1000 nm) window has deeper tissue penetration and higher resolution. Such excellent properties make NIR-II imaging-guided phototherapy an effective strategy for cancer treatment.[9–13] In order to achieve integrated diagnosis and treatment, the general strategy often requires several independent molecules with independent function to form nanomaterials. Such a complex encapsulation of different agents suffered from the disadvantages of early drug leakage, the

requirement of multiple laser sources, increased body burden, and a complex preparation process.[14,15] Therefore, it is urgent to develop NIR-II unimolecular probes for effective imaging-guided phototherapy.[16–18]

In recent years, some all-in-one phototheranostics have been reported for antitumor therapy.[19–25] However, this "always on" NIR-II phototheranostics inevitably leads to false positives, low tumor-normal tissue contrast, and damage to normal tissue. In contrast, activatable phototheranostics can respond to the tumor microenvironment (TME) or intracellular biomarkers (enzymes, pH, and active molecules), thereby effectively improving the accuracy of tumor diagnosis and making the treatment more controllable and safer.[26–31] Nitric oxide (NO) is an important intracellular and extracellular signaling molecule that participates in a variety of biological events such as immunity, and cardiovascular and neuronal communication.[29] It was reported that NO is overexpressed in the tumor microenvironment, which has been suggested to modulate different cancer-related events including the occurrence, invasion and metastasis of cancer.[30,31] Therefore, NO can be used as an effective active molecule to design "activatable" phototheranostics to achieve accurate diagnosis and specific treatment of tumors.[32–34]

Key Laboratory of Analytical Chemistry for Life Science of Shaanxi Province, Key Laboratory of Applied Surface and Colloid Chemistry, Ministry of Education, School of Chemistry and Chemical Engineering, Shaanxi Normal University, Xi'an, Shaanxi Province 710119, P. R. China. E-mail: yltang@snnu.edu.cn

Presently, some activatable NIR-II theranostic probes based on the nitric oxide response have been developed.[35–37] However, those probes only work through a single mechanism of photodynamic therapy (PDT) or photothermal therapy (PTT). Due to the hypoxic conditions of the tumor microenvironment and the presence of a large number of heat shock proteins (HSPs), the therapy effect of a single PDT/PTT strategy is still unsatisfactory.[38,39] Some recent research has indicated that with the help of ROS, the permeability of tumor cell membranes increases, which can accelerate the intracellular uptake of drugs and also make tumor cells more sensitive to heat, which is more conducive to PTT.[40–43] Thus, the combination of PDT and PTT can achieve a therapeutic effect of "1 + 1 > 2". However, until now, activatable phototheranostics with excellent fluorescence imaging ability, ROS generation ability and the photothermal effect for integrated precise diagnosis and treatment of tumors have not been reported.

Herein, we designed and synthesized a novel D–π–A–π–D NIR-II organic small molecule CTBA, which can be activated by nitric oxide for imaging-guided PDT/PTT synergistic tumor treatment (Scheme 1). Cyclopenta[2,1-b:3,4-b']dithiophene (CPDT) was selected as the electron donor unit, which has been widely used in the design of D–A polymers with excellent photodynamic properties.[44–47] At the same time, thiophene was added between the donor and the acceptor as a π bridge to extend the conjugation. The acceptor benzo[c][1,2,5]thiadiazole-5,6-diamine was used as not only the recognition group of nitric oxide but also as a reactive group to react with nitric oxide, which forms a triazole group with lower electron density.[48–50] When the electron density of the acceptor was greatly reduced, the emission wavelength of the probe molecule would be significantly red-shifted from the visible range to the NIR-II range. By rationally selecting the electron donor and the acceptor, the product activated by nitric oxide has excellent NIR-II fluorescence and photodynamic and photothermal properties. On the one hand, taking advantage of combined phototherapy, efficient tumor treatment can be achieved. On the other hand, with the characteristic of specific response, the diagnostic accuracy of tumors and the safety of the treatment process can be significantly improved. Then, CTBA-NPs were
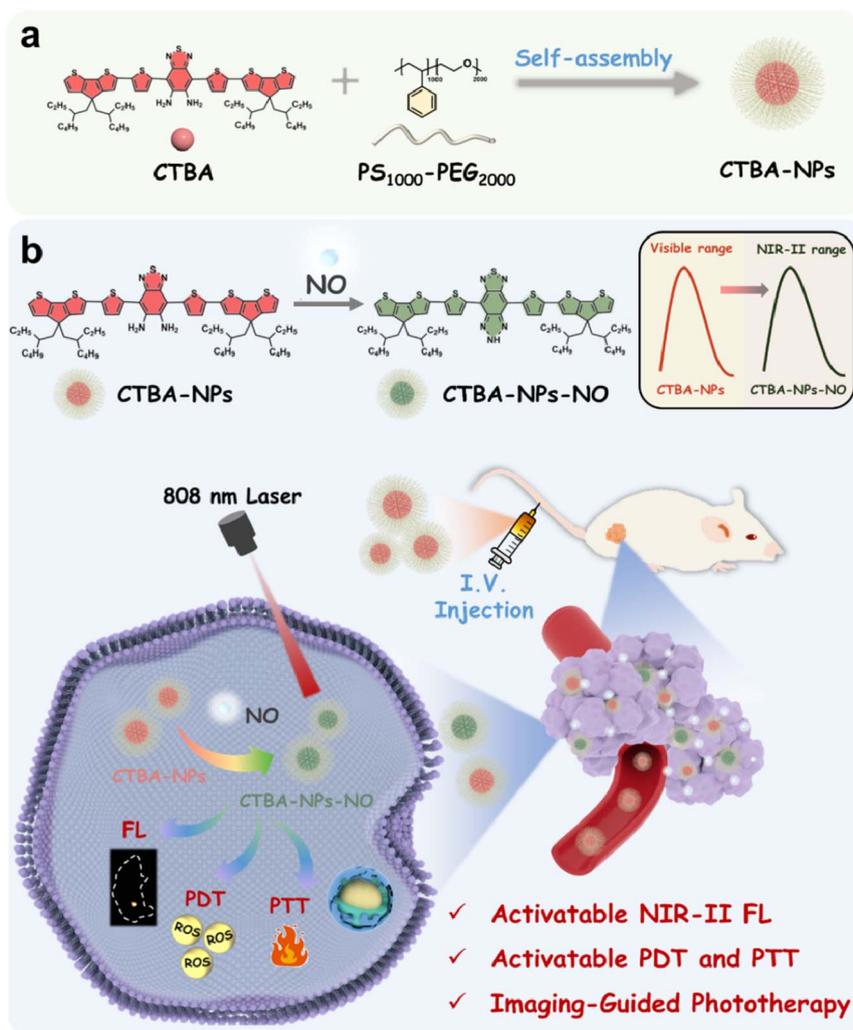
Scheme 1 (a) Preparation scheme of CTBA-NPs. (b) Mechanism of the activatable NIR-II fluorescent CTBA-NPs imaging-guided synergistic PDT/PTT treatment.

constructed by self-assembly between CTBA and PS$_{1000}$–PEG$_{2000}$. The activatable NIR-II imaging-guided PDT/PTT combined phototherapy was realized by such single-component nanoparticles. Finally, precise NIR-II imaging and effective treatment of mouse tumors were achieved based on CTBA-NPs.

Results and discussion

Design, synthesis and response characteristics to nitric oxide of CTBA

Benzo[c][1,2,5]thiadiazole-5,6-diamine is widely used in nitric oxide detection because it can react quickly with nitric oxide to form triazole derivatives. To obtain a fluorophore with NIR-II emission, we used it as an electron acceptor to couple with the electron donor cyclopenta[2,1-b:3,4-b′]dithiophene (CPDT) and thiophene, forming a D–π–A–π–D type organic fluorophore CTBA. As an electron donor, when CPDT combines with

a suitable electron acceptor, the probe can achieve a photodynamic or photothermal effect under laser excitation. The large electron density of CPDT can also ensure that the fluorophore emits in the near-infrared II region. Meanwhile, the introduced electron-rich thiophene unit acts as a π-spacer and increases electron delocalization. The synthesis route of CTBA is shown in Fig. 1a. The compound **3** was obtained via a Stille-coupling reaction followed by a bromination reaction. Then the donor unit and acceptor unit were also coupled together via a Stille-coupling reaction. The final product CTBA was obtained by the reduction reaction of zinc. The designed CTBA and the intermediates were successfully characterized by nuclear magnetic resonance (NMR) and matrix-assisted laser desorption ionization time-of-flight mass spectrometry (MALDI-TOF-MS) (Fig. S1–S12†). After the acceptor reacts with nitric oxide, CTBA can be converted into CTBT with a new structure, which in turn causes changes in photophysical properties (Fig. 1b). First, the changes
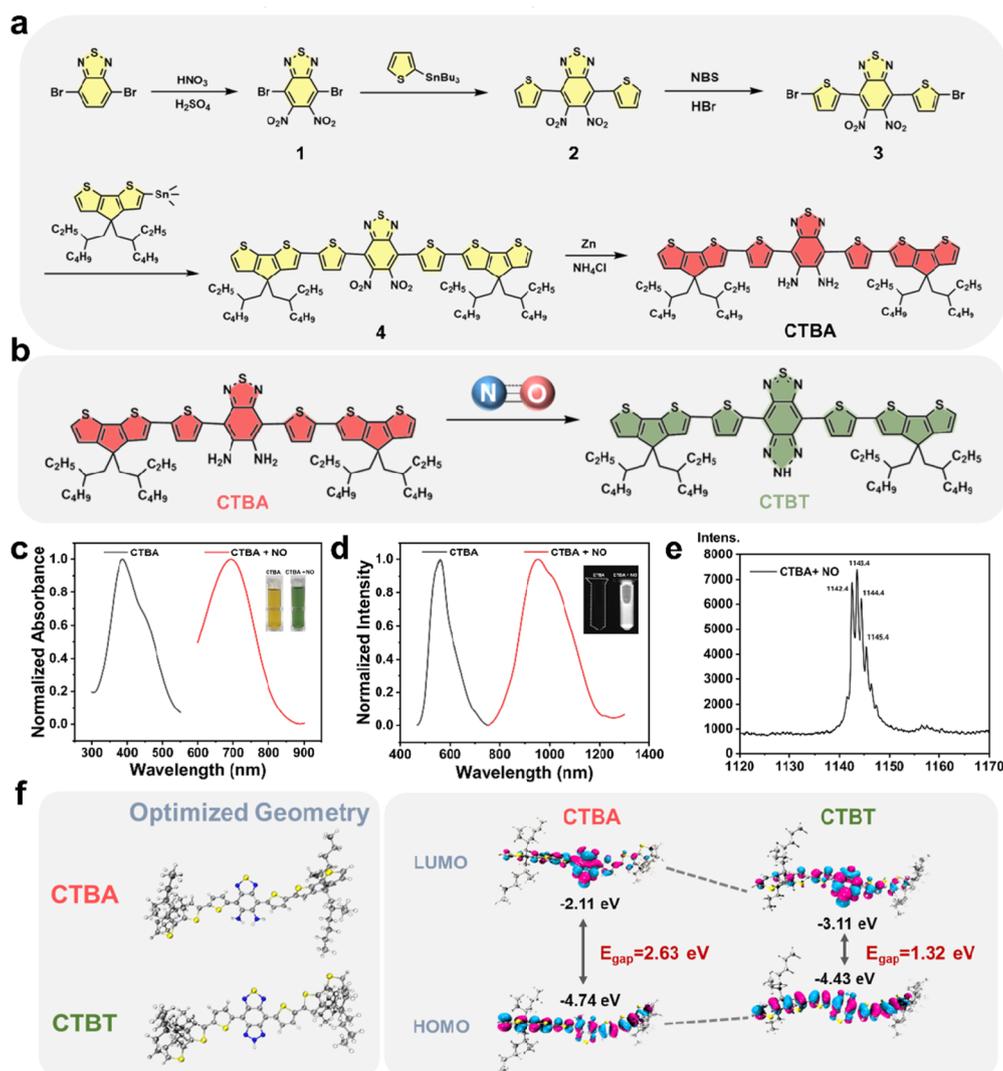

Fig. 1 (a) The synthesis route of CTBA. (b) The reaction of CTBA with NO. (c) Absorption spectra of CTBA before and after mixing with NO in THF (inset: image of CTBA solution with or without adding NO). (d) Fluorescence spectra of CTBA before and after mixing with NO in THF. λ_{ex}: 386 nm or 695 nm (inset: NIR-II image of CTBA solution with or without adding NO). (e) MALDI-TOF-MS spectrum of the reaction product of CTBA with NO. (f) Optimized geometries as well as the distribution and energy levels of LUMOs and HOMOs for the S$_0$ states of CTBA and CTBT.

in its spectral properties were characterized. As shown in Fig. 1c, CTBA exhibited an absorption range between 300 nm and 550 nm with a peak at around 385 nm. The emission spectrum spanned from 450 nm to 750 nm with the maximum emission at 560 nm. When benzo[c][1,2,5]thiadiazole-5,6-diamine is oxidized by nitric oxide to form a stronger acceptor 5H-[1,2,3]triazolo[4,5-f]-2,1,3-benzo-thiadiazole, the intra-molecular charge transfer (ICT) process is favored, which reduces the band gap of the entire fluorescence and achieves a significant red shift of the wavelength. Thus, when NO was added to CTBA solution, the absorption spectrum showed a great red shift to 600–900 nm. In the meantime, its emission spectrum shifts to the NIR-II window of 800–1200 nm, accompanied by strong NIR-II fluorescence (Fig. 1d). MALDI-TOF-MS was used to confirm the formation of products after the reaction of CTBA and NO. As shown in Fig. 1e, when CTBA was mixed with NO, the mass spectrum peak at ~1143 belonging to the triazole derivative product CTBT was observed.

In order to explore the reason for the changes in the spectral properties of the probe before and after the reaction with nitric oxide, density functional theory (DFT) calculation was performed to investigate the geometric conformation and electronic properties of CTBA and CTBT. As shown in Fig. 1f, the

highest occupied molecular orbital (HOMO) was mainly distributed throughout the entire conjugated backbone, while the lowest unoccupied molecular orbital (LUMO) tends to be distributed in the acceptors. This indicates that both CTBA and CTBT have obvious donor–acceptor interactions and intramolecular charge transfer. It is worth noting that since the acceptor in CTBT has a stronger electron-withdrawing ability, the electrons in its LUMO are more concentrated in the acceptor part compared with CTBA. Such electron distribution characteristics cause the electronic energy level of its LUMO to decrease from −2.11 eV to −3.11 eV. At the same time, accompanied by a partial increase in the HOMO, the HOMO–LUMO energy gap of CTBT is ultimately reduced to 1.32 eV. A narrower band gap can more easily achieve longer wavelength absorption, which is consistent with the significant spectral red shift. The changes in spectral properties indicate that CTBA can be used as an ideal NIR-II fluorescent probe for the detection of NO.

Preparation, photophysical properties and response of CTBA-NPs to nitric oxide

To enhance the biocompatibility for biomedical applications, the nano-co-precipitation method was used to construct the
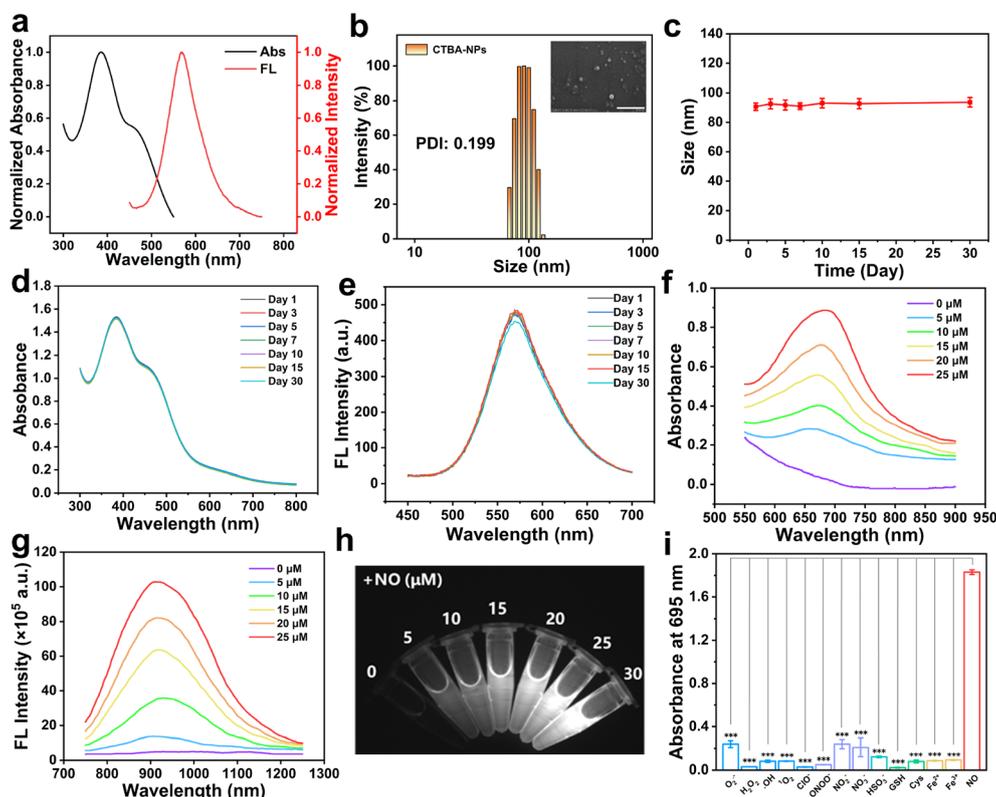

Fig. 2 (a) Absorption and fluorescence spectra of CTBA-NPs in H$_2$O (λ_{ex}: 386 nm). (b) Hydrated diameter of the CTBA-NPs (inset: SEM image of CTBA-NPs. Scale bar: 500 nm). Hydrated diameter (c), and absorption (d) and fluorescence (e) spectra of CTBA-NPs stored in H$_2$O for 30 days. (f) Absorbance spectra of CTBA-NPs (25 μM) responsive to different concentrations of NO. (g) Fluorescence spectra of CTBA-NPs (25 μM) responsive to different concentrations of NO. (h) NIR-II fluorescence images of CTBA-NPs with different concentrations of NO added (λ_{ex}: 808 nm, 0.3 W cm^{-2}, 1000 nm long-pass filter, 5 ms). (i) Absorbance at 695 nm of the CTBA-NPs in the presence of O$_2^{\bullet-}$ (250 μM), H$_2$O$_2$ (250 μM), $^{\bullet}$OH (250 μM), ^{1}O$_2$ (250 μM), ClO$^-$ (250 μM), ONOO$^-$ (250 μM), NO$_2^-$ (250 μM), NO$_3^-$ (250 μM), HSO$_3^-$ (250 μM), GSH (250 μM), Cys (250 μM), Fe^{2+} (250 μM), Fe^{3+} (250 μM), and NO (50 μM). Data are presented as the mean ± SD (n = 3). (***) P < 0.001.

CTBA-NPs by encapsulating CTBA with PS_{1000}–PEG_{2000}. Subsequently, the photophysical properties of CTBA-NPs were examined. As shown in Fig. 2a, the spectra of CTBA-NPs were similar to those of CTBA with an absorbance from 300 nm to 550 nm and emission from 500 nm to 750 nm. Fig. 2b shows that the hydrated particle size of CTBA-NPs was ~96 nm. The scanning electron microscope (SEM) image showed that the morphology of CTBA-NPs was spherical and uniform. After being stored in water for 30 days, the particle size, and absorption and fluorescence spectrum of CTBA-NPs did not change significantly, proving that it has good colloid stability (Fig. 2c–e). In addition, the stability of CTBA-NPs under biological conditions was also evaluated. Both the spectral properties and the particle size did not change significantly within 7 days, confirming its excellent systematic stability (Fig. S13†). Next, the optical properties of CTBA-NPs towards NO were studied. Without NO, no absorption peak at 695 nm was observed. However, after the addition of NO, the absorption peak appeared here and continued to increase with the increase in NO (Fig. 2f), which showed a good linear relationship with the NO concentration in the concentration range of 0–25 μM (Fig. S14a†). Correspondingly, the emission intensity of CTBA-NPs at 925 nm also increased with

NO concentration, showing a great linear relationship (Fig. 2g and S14b†). Similarly, with the increase in NO concentration, the signal intensity of NIR-II fluorescence imaging also gradually increases (Fig. 2h). The changes in absorption spectra and NIR-II fluorescence signals of CTBA-NPs after the addition of NO are attributed to the oxidation of the *o*-phenylenediamine acceptor group by NO into a stronger acceptor, which strengthens the ICT process of the entire molecule.

Furthermore, to explore the duration of the reaction between CTBA-NPs and NO, excess NO was added to the CTBA-NPs solution and its absorption and emission spectra were measured at different times. As shown in Fig. S15,† with the extension of time, the absorbance of CTBA-NPs at 695 nm and the intensity at 925 nm gradually increased and reached a plateau at 4 h, confirming that CTBA-NPs can completely react with exogenous NO within 4 h. At the same time, the response rates under different pH conditions were also tested. As shown in Fig. S16,† CTBA-NPs can be activated more quickly under acidic conditions. Therefore, the acidic microenvironment of tumor tissue is more conducive to the occurrence of this activation process. To test the specificity of CTBA-NPs in response to NO, CTBA-NPs were treated with a panel of biologically relevant analytes, such as reactive oxygen species,
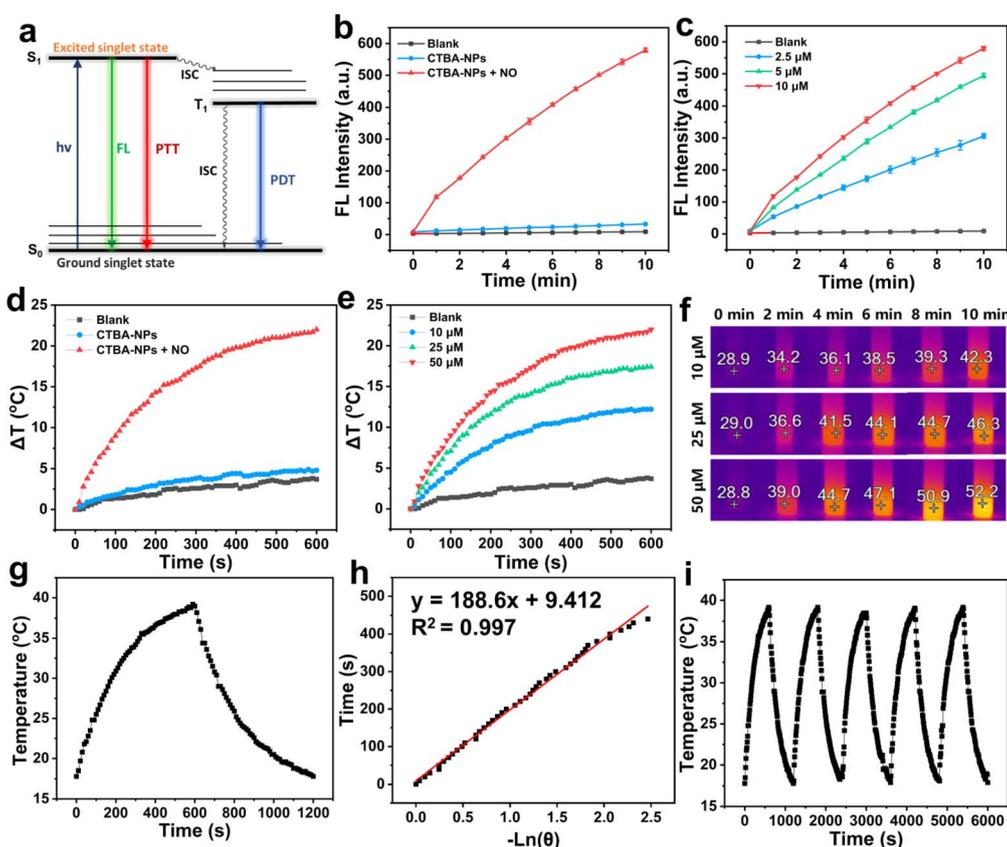

Fig. 3 (a) Jablonski diagram. (b) ROS generation of CTBA-NPs with and without NO under an 808 nm laser (0.8 W cm^{-2}) for 10 min. (c) ROS generation of CTBA-NPs of different concentrations with NO under an 808 nm laser (0.8 W cm^{-2}) for 10 min, as quantified using DCFH (40 μM, λ_{ex}: 488 nm, λ_{em}: 525 nm) as a probe. (d) Photothermal effect of CTBA-NPs with and without NO under an 808 nm laser (0.8 W cm^{-2}) for 10 min. (e) Photothermal effect of CTBA-NPs of different concentrations with NO under an 808 nm laser (0.8 W cm^{-2}) for 10 min. (f) The temperature of CTBA-NPs of different concentrations under an 808 nm laser (0.8 W cm^{-2}) for 10 min. (g) One cycle of the irradiation on/off treatment. (h) The cooling time *versus* the negative natural logarithm of the temperature obtained from the cooling stage. (i) Temperature rising and cooling profiles of CTBA-NPs with irradiation on/off for five cycles.

reactive nitrogen species, proteins and metal ions. As shown in Fig. 2i, the absorption at 695 nm was enhanced significantly only in the presence of NO, while it remained unchanged after incubating with other interferents, indicating that CTBA-NPs had a high selectivity for NO.

Photodynamic and photothermal properties of CTBA-NPs

As shown in the Jablonski molecular energy level diagram (Fig. 3a), in addition to the fluorescence produced by the radiative-leap pathway, the non-radiative-leap and inter-system crossing (ISC) pathways may also produce effective photothermal or photodynamic effects. Thus, the phototherapeutic abilities of CTBA-NPs before and after interaction with nitric oxide were evaluated. First, to detect the ROS generated by near-infrared light excitation, 2′,7′-dichlorodihydrofluorescein (DCFH-DA) was used as an indicator. In the presence of ROS, DCFH-DA is oxidized to 2,7-dichlorofluorescein (DCF) with high fluorescence. As shown in Fig. 3b, c and S17,† CTBA-NPs produce almost no ROS under 808 nm laser irradiation because the absorption at 808 nm is negligible without nitric oxide. However, when fully reacted with NO to form the product CTBT, a large amount of ROS generation can be observed at a concentration of 2.5 μM. When the concentration reaches 10 μM, the ROS production can reach about 70 times more than that of the blank. This indicates that CTBA-NPs had a significant photodynamic effect when activated by nitric oxide. In order to identify the type of ROS, 9,10-anthracenediyl-bis(methylene)bismalonic acid (ABDA), dihydrorhodamine 123 (DHR123) and hydroxyphenyl fluorescein (HPF) were used to detect $^1O_2$, $^{\cdot}O_2^-$ and $^{\cdot}OH$, respectively. As shown in Fig. S18a,† the absorbance of ABDA hardly changed during the 6 min irradiation. This result indicated that $^1O_2$ was not produced through the type II pathway. In contrast, under laser irradiation, the fluorescence intensity of DHR123 and HPF increased significantly within 6 min, reflecting the excellent $^{\cdot}O_2^-$ and $^{\cdot}OH$ generation ability via the type I pathway (Fig. S18b and c†). Besides, the photothermal capability of CTBA-NPs was also evaluated (Fig. 3d–f). When not activated by NO, CTBA-NPs showed no obvious thermal effect under 808 nm laser irradiation. However, after being activated by NO, the temperature of 10 μM, 25 μM and 50 μM CTBA-NPs solution increased by 12.2 °C, 17.4 °C and 22.1 °C within 10 min, respectively. Furthermore, the photothermal conversion efficiency of CTBA-NPs activated by NO was investigated. As shown in Fig. 3g, within 10 minutes, the temperature of CTBA-NPs gradually increased under 808 nm laser irradiation, and then it gradually returned to room temperature naturally. Afterward, the photothermal conversion efficiency η was calculated to be 22.3% according to the fitting curve in Fig. 3h and the formula. Photothermal stability is an important basis for determining whether photothermal reagents are suitable for further biological applications. Therefore, we tested the photo-thermal stability of CTBA-NPs activated by NO. As shown in Fig. 3i, during the five cycles of laser switching, the rising and falling trends of the solution temperature did not show obvious changes. The above results showed that CTBA-NPs activated by NO had a good

photothermal capability and significant photothermal stability. Briefly, the in vitro ROS generation and photothermal effect investigation showed that CTBA-NPs had almost no phototherapy effect before being activated by NO. However, after being activated by NO, CTBA-NPs had an excellent phototherapy effect under 808 nm laser irradiation. Therefore, such a "turn-on" strategy makes it more controllable in further application in tumor treatment.

In vitro biocompatibility and antitumor efficiency of CTBA-NPs

First, the biocompatibility of CTBA-NPs in vitro was evaluated by MTT. Normal cell HUVEC (human umbilical vein endothelial cells) and cancer cells HepG2 (human liver cancer cells) and H22 (mouse liver cancer cells) were selected to evaluate their cell viability after incubation with CTBA-NPs. As shown in Fig. 4a, when treated with different concentrations of CTBA-NPs (0–100 μM), the survival rates of the three kinds of cells were all above 80%. This indicated that CTBA-NPs have excellent in vitro biocompatibility and can be used further for in vivo applications. Next, the cellular uptake performance of CTBA-NPs in HepG2 cells was evaluated. As shown in Fig. 4b and c, after incubating CTBA-NPs with HepG2 cells, time-dependent cellular uptake can be clearly observed by CLSM (Confocal Laser Scanning Microscopy). CTBA-NPs can obviously be taken up by HepG2 cells at 8 h and the uptake was complete at 12 h, which showed that CTBA-NPs can be well internalized by cells, enabling further exploration of phototherapy. Since CTBA-NPs can be effectively activated by nitric oxide, the toxicity of CTBA-NPs towards different cancer cells was evaluated under different conditions. As shown in Fig. 4d and e, when CTBN-NPs were not activated by nitric oxide, the cell viability of HepG2 and H22 cells could still be maintained above 80% under 808 nm laser irradiation. Similarly, when CTBN-NPs were activated by nitric oxide but not irradiated by 808 nm laser, the toxicity to both cells was also low. This indicated that CTBA-NPs will not cause cell damage in the absence of excessive nitric oxide and laser irradiation, ensuring its biosafety for normal tissues. Conversely, after being activated by nitric oxide, the cell viability of HepG2 and H22 was ~23% and ~21%, respectively, when the concentration of CTBA-NPs was 50 μM. This is because when activated by nitric oxide, CTBA-NPs showed significant photodynamic and photothermal effects under 808 nm laser irradiation, leading to damage and apoptosis of tumor cells. To further confirm this result, we performed the fluorescence imaging experiments after calcein acetoxymethyl ester (calcein AM)/propidium iodide (PI) double staining. As shown in Fig. 4f, CTBA-NPs could kill tumor cells under 808 nm laser irradiation only after being activated by nitric oxide, which was consistent with the MTT staining results. Next, the ability of activated CTBA-NPs to generate ROS in HepG2 cells was verified. The ROS levels in HepG2 cells after different treatments were detected by DCFH-DA. As shown in Fig. 4g, it can be clearly observed that the group with the addition of nitric oxide and 808 nm laser irradiation produced obvious green fluorescence, confirming that the activated CTBA-NPs can kill tumor cells through photodynamic action under
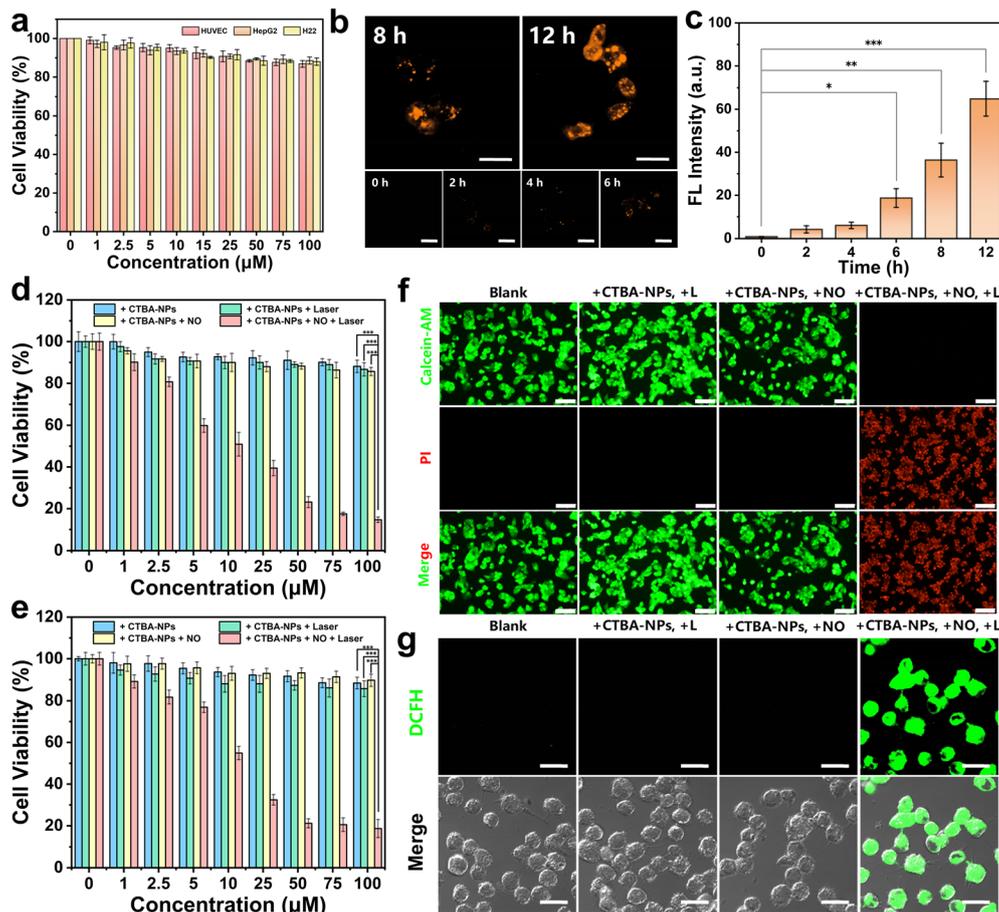
Fig. 4 (a) *In vitro* viability of HUVEC, HepG2, and H22 cells treated with CTBA-NPs at different concentrations. (b) CLSM images (scale bars: 30 μm) and (c) quantitative data of HepG2 cells after incubation with CTBA-NPs (25 μM). Cytotoxicity of CTBA-NPs at different concentrations against (d) HepG2 cells and (e) H22 cells without irradiation or under an 808 nm laser (0.8 W cm^{-2}) for 10 min. (f) Live/dead staining of HepG2 cells treated with CTBA-NPs (25 μM) with or without NO and 808 nm laser (0.8 W cm^{-2}) irradiation. The fluorescence images of calcein AM (4 μM) and PI (9 μM) were obtained using an inverted fluorescence microscope. Scale bars: 100 μm. (g) Fluorescence imaging of ROS generation ability of CTBA-NPs with or without NO and 808 nm laser (0.8 W cm^{-2}) irradiation in HepG2 cells. The fluorescence images were collected at 525−575 nm (λ_{ex}: 488 nm). Scale bars: 20 μm. Data are presented as the mean ± SD ($n = 5$). (*) $P < 0.05$, (**) $P < 0.01$, and (***) $P < 0.001$.

laser irradiation. Therefore, this activatable phototherapy system presented excellent biocompatibility for normal cells as well as great ability to kill tumor cells.

In vivo biosecurity and pharmacokinetics of CTBA-NPs

Furthermore, the preliminary *in vivo* safety experiments were conducted in BALA/c mice. Healthy BALB/C mice were randomly divided into three groups ($n = 3$). As shown in Fig. 5a, the mice were injected with different concentrations (0, 25 or 100 μM) of CTBA-NPs through the tail vein on day 1, day 5 and day 9. The mice were weighed and observed for signs of illness every other day. As shown in Fig. 5b, the changes in body weight of mice did not show significant abnormalities compared to the control group. After 14 days, the blood was obtained by blood collection through the retro-orbital venous plexus, partly by adding anticoagulant EDTA-K2 and partly by centrifugation to obtain serum for complete blood-cell counting and the biochemical indicator test. As shown in Fig. 5c–e, the white blood cells (WBCs), red blood cells (RBCs) and platelets (PLT)

were not significantly changed by CTBA-NPs treatment. These results suggested that CTBA-NPs did not produce inflammatory or hematologic diseases in mice. The results of albumin (ALB), aspartate aminotransferase (AST) and alanine transaminase (ALT) indicated that CTBA-NPs did not show significant hepatotoxicity (Fig. 5f–h). Similarly, the detection of blood urea nitrogen (BUN) and blood creatinine (CREA) confirmed that CTBA-NPs also showed no significant nephrotoxicity in mice (Fig. 5i and j).

Then the mice were euthanized and the major organs were isolated. The collected organs were fixed with 4% formaldehyde for H&E staining. As shown in Fig. 5k, the staining results of each organ did not show any obvious abnormality, which indicated that CTBA-NPs had excellent *in vivo* biosafety and can be further used for *in vivo* imaging and therapeutics. In addition, the distribution of CTBA-NPs *in vivo* was also studied. As shown in Fig. S19,† the fluorescence mainly appeared in the stomach, intestines, and colon at 1 h after being injected with CTBA-NPs. In the following 4 h to 48 h, the fluorescence signal
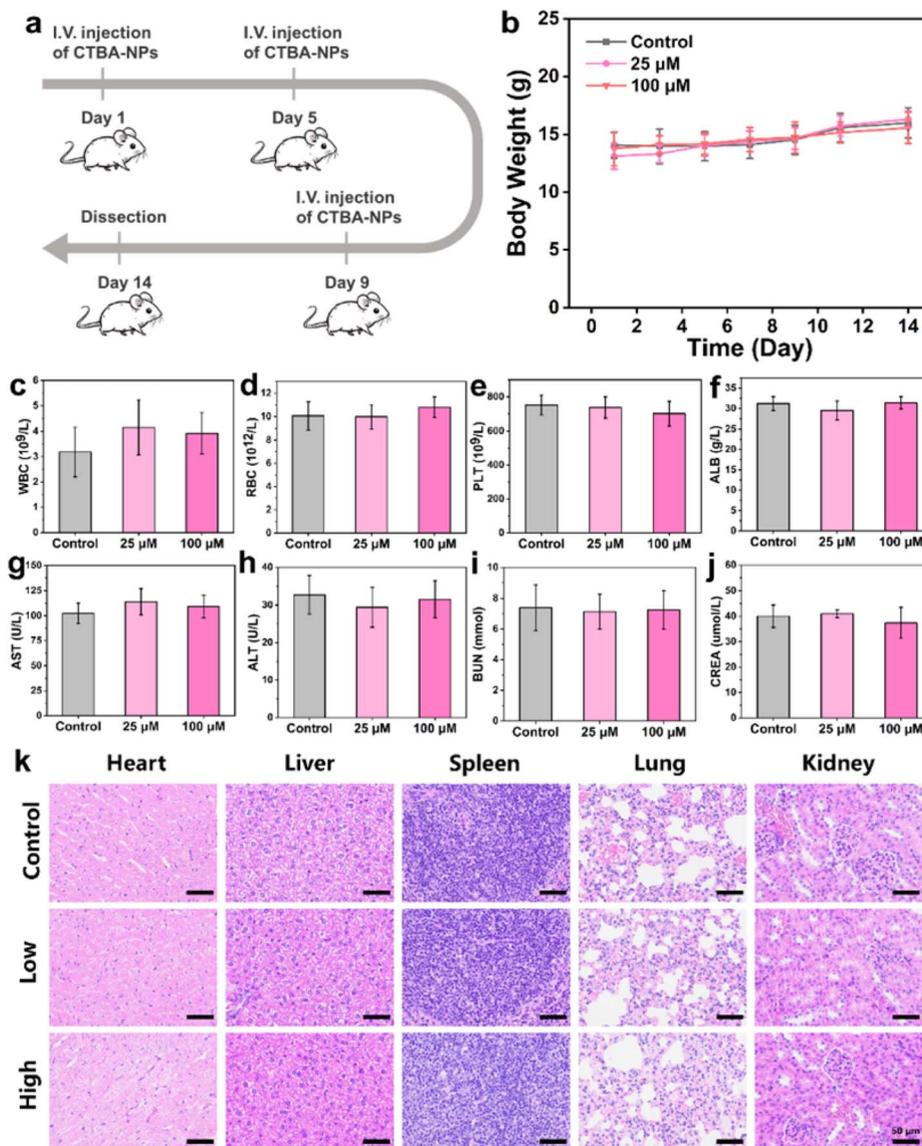
Fig. 5 Safety profiles of CTBA-NPs in BALB/C mice during 14 days of intravenous injection. (a) The experimental protocols. (b) Changes in body weight during 14 days with various treatments. Data are presented as the mean ± SD ($n = 3$). Changes in WBC (c), RBC (d), PLT (e), ALB (f), AST (g), ALT (h), BUN (i), and CREA (j) after 14 days with various treatments. Data are presented as the mean ± SD ($n = 3$). (k) Hematoxylin and eosin (H&E) staining for the main organs extracted from the mice at the end of different treatments (low: [CTBA-NPs] = 25 µM; high: [CTBA-NPs] = 100 µM). Scale bars: 50 µm.

first increased and then gradually weakened. This confirmed that CTBA-NPs mainly accumulated in some organs with dense blood vessels in the digestive system and were gradually excreted over time. Combined with the above results, CTBA-NPs have low metabolic toxicity *in vivo*, which is conducive to biological imaging.

In vivo tumor imaging in the NIR-II window of CTBA-NPs

Since the property of penetrating deep tissues is crucial for NIR-II imaging, the tissue penetration ability of CTBA-NPs was evaluated before applying it to *in vivo* imaging. As shown in Fig. 6a, when CTBA-NPs fully reacted with nitric oxide, it led to bright NIR-II fluorescence. When no chicken tissue was added

for coverage, the brightness of CTBA-NPs and ICG was consistent on adjusting the concentration under the same imaging conditions. When the thickness of the tissue gradually increased, the signal intensity of ICG decreased significantly, accompanied by a decrease in the signal-to-background ratio (SBR) and an increase in the full width at half maximum (FWHM), significantly reducing the imaging resolution (Fig. 6b, c and S20†). In contrast, when the tissue thickness was less than 4 mm, the fluorescence signal of CTBA-NPs can still maintain an SBR greater than 2. When the tissue thickness increased to 6 mm, the fluorescence signal belonging to CTBA-NPs can also be observed. In general, the SBR and FWHM of CTBA-NPs for NIR-II imaging were better than those of ICG. All the results indicated that CTBA-NPs can be used for ideal NIR-II *in vivo*
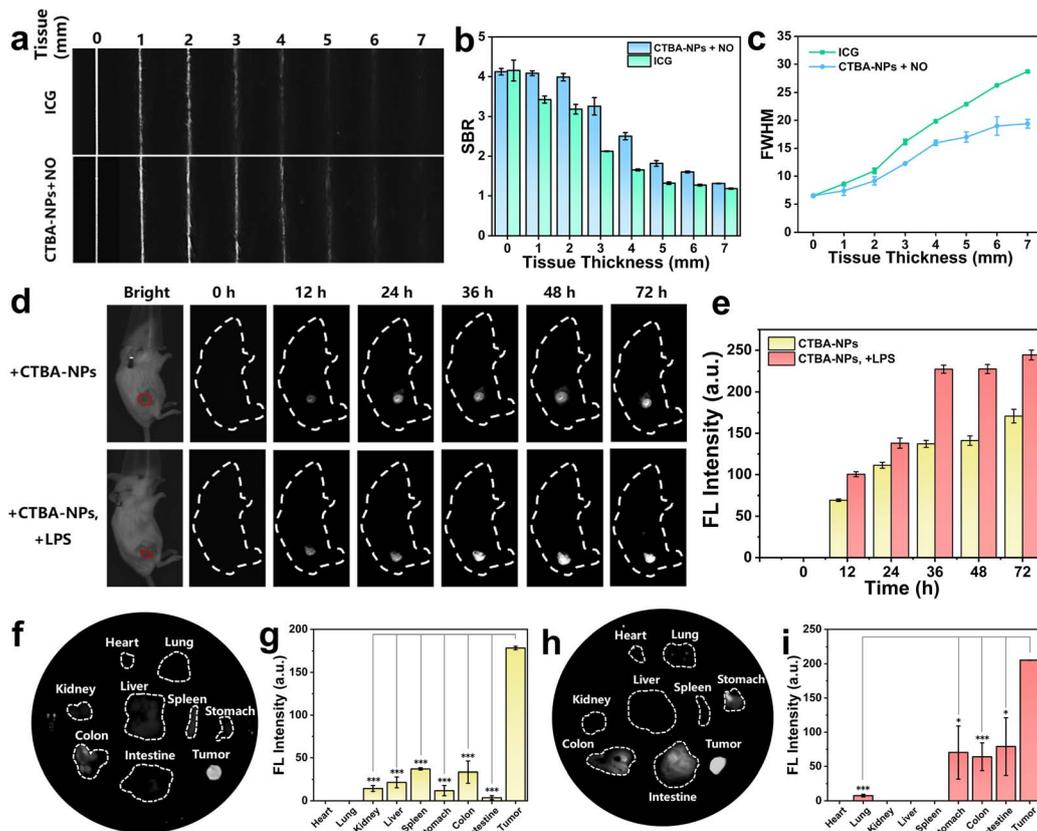
Fig. 6 (a) NIR-II fluorescence images of CTBA-NPs with NO and ICG covered with different thicknesses (0–7 mm) of chicken breast tissue (λ_{ex}: 808 nm, 0.3 W cm^{-2}, 900 nm long-pass filter, 10 ms). (b) SBR calculation for the capillary tube in (a). (c) The full widths at half-maximum (FWHM) of the capillary tube in (a). (d) NIR-II images obtained from the back position of a tumor-bearing BALB/C mouse at different time after CTBA-NPs intravenous injection (λ_{ex}: 808 nm, 0.3 W cm^{-2}, 900 nm long-pass filter, 50 ms). (e) The corresponding NIR-II signal intensity of (d). (f) NIR-II images of dissected organs and tumors at 72 h of the BALB/C mouse after CTBA-NPs intravenous injection (λ_{ex}: 808 nm, 0.3 W cm^{-2}, 900 nm long-pass filter, 30 ms). (g) The corresponding NIR-II signal intensity of (f). (h) NIR-II images of dissected organs and tumors at 72 h of the BALB/C mouse after CTBA-NPs intravenous injection and LPS intratumor injection (λ_{ex}: 808 nm, 0.3 W cm^{-2}, 900 nm long-pass filter, 30 ms). (i) The corresponding NIR-II signal intensity of (h). Data are presented as the mean ± SD ($n = 3$). (*) $P < 0.05$ and (***) $P < 0.001$.

imaging. Next, CTBA-NPs were applied to the NIR-II imaging of the tumor in mice. CTBA-NPs can be enriched in the tumor site through the enhanced permeability and retention (EPR) effect and activated by the excess nitric oxide in the tumor microenvironment. The activated product showed obvious NIR-II fluorescence under 808 nm laser irradiation. As shown in Fig. 6d and e, obvious fluorescence emission can be observed in the tumor site at 12 h. As more CTBA-NPs were enriched in the tumor and the activation of nitric oxide was enhanced, the fluorescence intensity gradually increased within 72 h. It is worth noting that the NIR-II fluorescence of CTBA-NPs was specifically activated by nitric oxide, whereas the background signal during imaging was unobservable. This indicated that the nanofluorescent CTBA-NPs activated by nitric oxide can achieve sensitive and precise NIR-II imaging of tumors. In addition, when lipopolysaccharide (LPS) solution was injected intratumorally to stimulate inflammation and produce more nitric oxide, the fluorescence intensity was also significantly enhanced, which further confirmed that the NIR-II fluorescence of CTBA-NPs was indeed activated by nitric oxide. Finally, the mice were sacrificed and dissected for NIR-II tumor imaging,

and *ex vivo* NIR-II fluorescence imaging of their major organs and tumors was performed. As shown in Fig. 6f–i, due to the specificity of activation imaging, no obvious NIR-II fluorescence signals were observed in the main organs of the mice. After LPS stimulation, there were weak fluorescence signals in the stomach and intestines of the mice, which may be caused by the further metabolism of CTBA-NPs activated in the tumor site through the digestive system. However, because its fluorescence signal is very low compared to that of tumor tissue, it will not affect the accuracy of NIR-II imaging during *in vivo* tumor imaging. These results indicated that CTBA-NPs can be used as excellent NIR-II tumor imaging agents for tumor diagnosis and tumor treatment due to the ability of specific activation by nitric oxide.

In vivo antitumor efficiency of CTBA-NPs

To verify the phototherapeutic potential of CTBA-NPs, the *in vivo* antitumor effects were subsequently evaluated in H22 tumor-bearing mice. As shown in Fig. 7a, H22 cells were subcutaneously inoculated into BALB/C mice. When the tumor
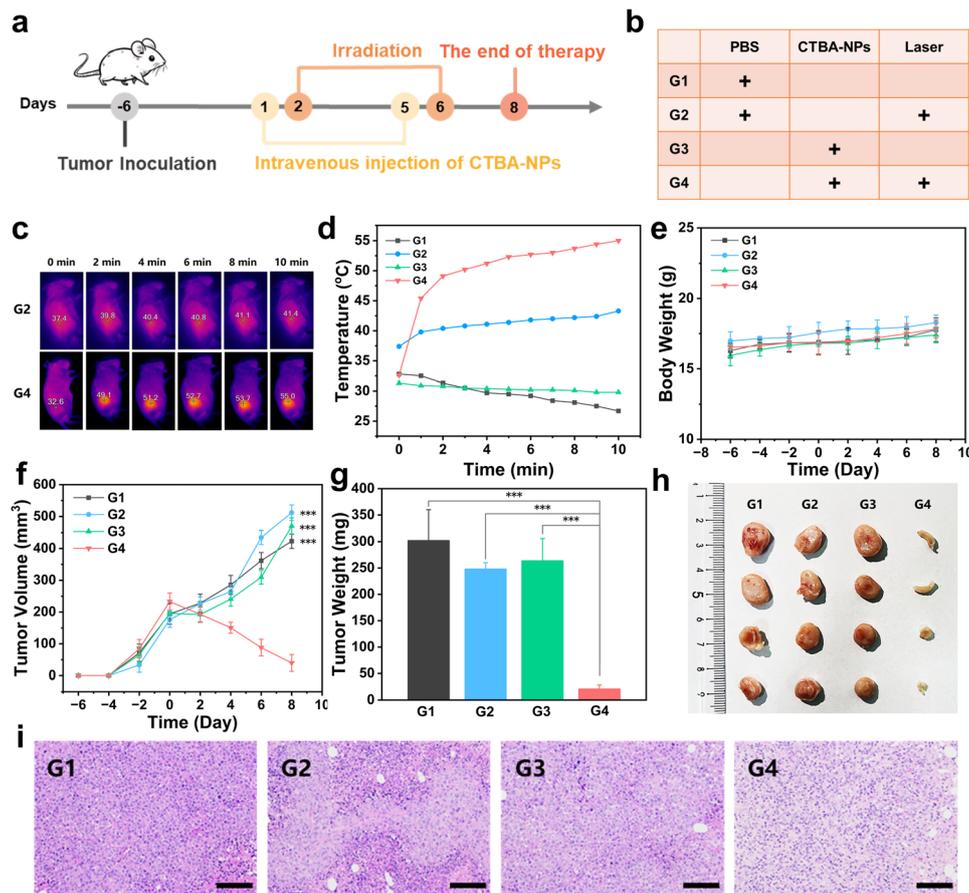
Fig. 7 The antitumor efficacy of CTBA-NPs in H22 tumor-bearing mice. (a) Schematic treatment protocol of the *in vivo* therapeutic process. (b) Different treatments: PBS (G1), PBS with laser irradiation (G2), CTBA-NPs without laser irradiation (G3), and CTBA-NPs with laser irradiation (G4). (c) Infrared thermal images of the mice at different points with different treatments ($\lambda_{ex} = 808$ nm, 0.8 W cm^{-2}). (d) The temperature of the mice at different points with various treatments ($\lambda_{ex} = 808$ nm, 0.8 W cm^{-2}). (e) Body weight of the mice with various treatments ($n = 4$). (f) Tumor growth curves of each group. (g) Tumor weight of the mice with various treatments ($n = 4$). (h) Representative photographs of the tumors extracted from the mice in each group. (i) H&E staining of tumors in various groups at the end of the treatments. Scale bar: 100 μm. (***) $P < 0.001$.

grew up to 200 ± 50 mm^3, the tumor-bearing mice were randomly divided into six groups with four mice per group: the (1) PBS-treated group; (2) PBS-treated with laser group; (3) CTBA-NPs-treated group; (4) CTBA-NPs-treated with laser group (Fig. 7b). As shown in Fig. 7c and d, after being activated by excessive nitric oxide in the tumor microenvironment, CTBA-NPs showed an obvious photothermal effect under 808 nm laser irradiation. The temperature of the tumor site can increase by more than 20 °C, which is consistent with the result of *in vitro* photothermal experiments. The body weight and tumor volume of each group were measured every 2 days from tumor inoculation. As shown in Fig. 7e, there was no significant difference in the body weight of mice in each group. As shown in Fig. 7f–h and S21,† the tumors in the G1, G2 and G3 groups grew rapidly without obvious inhibitory effects, indicating that single 808 nm laser irradiation or injection of CTBA-NPs could not kill tumor cells. Notably, when CTBA-NPs and 808 nm laser were used for collaborative treatment, the tumor volume was significantly reduced or even disappeared. This phenomenon can be attributed to the fact that CTBA-NPs activated by nitric oxide

generated cytotoxic ROS under laser irradiation, exhibiting significant photothermal effects. In addition, H&E staining of tumors in different groups after treatment further evaluated the anti-tumor ability of CTBA-NPs. As shown in Fig. 7i, the tumor tissue images of the treatment group showed obvious cell nucleus damage under light excitation, indicating cell apoptosis and necrosis. In addition, digital photos and H&E staining of the main organs of mice in each group showed no pathological abnormalities (Fig. S22 and S23†), which was attributed to the excellent biocompatibility of CTBA-NPs and the safety and controllability of the "activatable" strategy. In conclusion, the activatable phototherapy system demonstrated significant tumor-ablation capabilities with excellent biosafety.

Conclusion

In summary, we designed and synthesized a D–π–A–π–D type NIR-II integrated diagnostic and therapeutic fluorescent probe that can be activated by nitric oxide. The high electron density electron donor CPDT was used to combine with the nitric oxide

responsive group benzo[*c*][1,2,5]thiadiazole-5,6-diamine acceptor to obtain the small molecule fluorophore CTBA. Furthermore, CTBA-NPs were formed by encapsulating CTBA with PS_{1000}–PEG_{2000}. When CTBA-NPs were activated by excessive nitric oxide in the tumor microenvironment, the *o*-phenylenediamine group of the acceptor part can convert into a triazole group with lower electron density. Therefore, the emission wavelength of the probe will significantly red-shift from white light to the NIR-II window. At the same time, under 808 nm laser irradiation, it exhibited significant photodynamic and photothermal properties. Notably, the activatable CTBA-NPs were successfully applied to the precise NIR-II imaging and PDT/PTT synergistic therapy for mouse tumors. This work paves the way for the design of activatable NIR-II probes and provides a new strategy for precise diagnosis and imaging-guided synergistic phototherapy of tumors.

Ethical statement

All animal procedures were performed in accordance with the Guidelines for Care and Use of Laboratory Animals of Shaanxi Normal University and approved by the Animal Ethics Committee of Shaanxi Normal University, CE-2024-0012-BG6.

Data availability

The data supporting this article have been included in the main text and the ESI.†

Author contributions

X. Y. Z. and Y. L. T. conceived the project. X. Y. Z., Y. X. R., X. Y. M., Y. J. L., and J. Q. W. performed the experiments. Y. L. T. supervised the research. X. Y. Z., L. L., and M. Q. L. analyzed the data. X. Y. Z. and Y. L. T. wrote and revised the paper. Y. L. T. performed validation, and reviewed and edited the writing. All the authors discussed the results and contributed to the preparation of the manuscript.

Conflicts of interest

There are no conflicts to declare.

Acknowledgements

Notes and references

1 C. Allemani, H. K. Weir, H. Carreira, R. Harewood, D. Spika, X.-S. Wang, F. Bannon, J. V. Ahn, C. J. Johnson, A. Bonaventure, R. Marcos-Gragera, C. Stiller, G. Azevedo e Silva, W.-Q. Chen, O. J. Ogunbiyi, B. Rachet, M. J. Soeberg, H. You, T. Matsuda, M. Bielska-Lasota, H. Storm, T. C. Tucker and M. P. Coleman, *Lancet*, 2015, **385**, 977–1010.

2 M. Gao, F. Yu, C. Lv, J. Choo and L. Chen, *Chem. Soc. Rev.*, 2017, **46**, 2237–2271.

3 E. S. Reis, D. C. Mastellos, D. Ricklin, A. Mantovani and J. D. Lambris, *Nat. Rev. Immunol.*, 2018, **18**, 5–18.

4 V. J. N. Bykov, S. E. Eriksson, J. Bianchi and K. G. Wiman, *Nat. Rev. Cancer*, 2018, **18**, 89–102.

5 S. Xia, H. Bai, E. Zhang, W. Yu, Z. Gao, F. Lv, Y. Huang, D. Zhu and S. Wang, *CCS Chem.*, 2023, **5**, 2324–2333.

6 R. L. Siegel, K. D. Miller, N. S. W. Mbbs and A. J. Dvm, *CA Cancer J. Clin.*, 2023, **73**, 17–48.

7 P. Cheng and K. Pu, *Nat. Rev. Mater.*, 2021, **6**, 1095–1113.

8 X. Tian, L. C. Murfin, L. Wu, S. E. Lewis and T. D. James, *Chem. Sci.*, 2021, **12**, 3406–3426.

9 F. Wang, Y. Zhong, O. Bruns, Y. Liang and H. Dai, *Nat. Photonics*, 2024, **18**, 535–547.

10 F. Ding, Y. Zhan, X. Lu and Y. Sun, *Chem. Sci.*, 2018, **9**, 4370–4380.

11 B. Wang, H. Zhou, L. Chen, Y. Ding, X. Zhang, H. Chen, H. Liu, P. Li, Y. Chen, C. Yin and Q. Fan, *Angew. Chem., Int. Ed.*, 2024, e202408874.

12 Z. Zhang, Y. Du, X. Shi, K. Wang, Q. Qu, Q. Liang, X. Ma, K. He, C. Chi, J. Tang, B. Liu, J. Ji, J. Wang, J. Dong, Z. Hu and J. Tian, *Nat. Rev. Clin. Oncol.*, 2024, **21**, 449–467.

13 X. Zhang, L. Li, Y. Ren, M. Li and Y. Tang, *Adv. Funct. Mater.*, 2025, **35**, 2413341.

14 Y. Zhang, S. Bo, T. Feng, X. Qin, Y. Wan, S. Jiang, C. Li, J. Lin, T. Wang, X. Zhou, Z. Jiang and P. Huang, *Adv. Mater.*, 2019, **31**, 1806444.

15 C. Chen, H. Ou, R. Liu and D. Ding, *Adv. Mater.*, 2020, **32**, 1806331.

16 X. Zhao, S. Long, M. Li, J. Cao, Y. Li, L. Guo, W. Sun, J. Du, J. Fan and X. Peng, *J. Am. Chem. Soc.*, 2020, **142**, 1510–1517.

17 H. Zhou, X. Zeng, A. Li, W. Zhou, L. Tang, W. Hu, Q. Fan, X. Meng, H. Deng, L. Duan, Y. Li, Z. Deng, X. Hong and Y. Xiao, *Nat. Commun.*, 2020, **11**, 6183.

18 Y. Wan, W. Chen, Y. Liu, K. Lee, Y. Gao, D. Zhang, Y. Li, Z. Huang, J. Luo, C. Lee and S. Li, *Adv. Mater.*, 2024, **36**, 2405966.

19 X. Hu, C. Zhang, J. Lv, R. Li, A. Qin, C. Zhu, F. Sun, Z. Chen, S. Teng, H. Lin, Z. Yang and W. Huang, *CCS Chem.*, 2025, 1–16.

20 Y. Ren, X. Zhang, L. Li, Q. Yuan, B. Bao, M. Li and Y. Tang, *Chem. Sci.*, 2025, **16**, 5089–5098.

21 D. Yan, Z. Zhang, J. Zhang, X. Li, Q. Wu, Y. Gui, J. Zhu, M. Kang, X. Chen, B. Z. Tang and D. Wang, *Angew. Chem., Int. Ed.*, 2024, **63**, e202401877.

22 P. Xiao, W. Xie, J. Zhang, Q. Wu, Z. Shen, C. Guo, Y. Wu, F. Wang, B. Z. Tang and D. Wang, *J. Am. Chem. Soc.*, 2023, **145**, 334–344.

23 B. Li, E. Pang, S. Zhao, G. Deng, S. Wang, B. Wang, J. Wu, G. Niu, X. Song and M. Lan, *Chem. Biomed. Imaging*, 2023, **1**, 541–549.

24 C. Wu, F. Zhang, Y. Mao, X. Qi, X. Wang, W. Zhang, B. Tang and P. Li, *Chem. Biomed. Imaging*, 2023, **1**, 372–379.

25 Q. Yu, J. Zhou, H. Wang, Y. Liu, H. Zhou, B. Kang, H. Chen and J. Xu, *Chem. Biomed. Imaging*, 2023, **1**, 242–250.

26 C. Zhang, M. Xu, Z. Zeng, X. Wei, S. He, J. Huang and K. Pu, *Angew. Chem., Int. Ed.*, 2023, **62**, e202217339.

27 M. Zhao, B. Li, H. Zhang and F. Zhang, *Chem. Sci.*, 2021, **12**, 3448–3459.

28 J. Sun, X. Cai, C. Wang, K. Du, W. Chen, F. Feng and S. Wang, *J. Am. Chem. Soc.*, 2021, **143**, 868–878.

29 J. Sun, K. Du, J. Diao, X. Cai, F. Feng and S. Wang, *Angew. Chem., Int. Ed.*, 2020, **59**, 12122–12128.

30 J. Song, H. Wang, X. Meng, W. Li and J. Qi, *Nat. Commun.*, 2024, **15**, 10395.

31 H. Zhou, Y. Zhang, R. Zhang, M. Zhao, W. Chen, Y. Liu, Y. Jiang, Q. Li, Q. Miao and M. Gao, *Adv. Mater.*, 2023, **35**, 2211485.

32 S. Korde Choudhari, M. Chaudhary, S. Bagde, A. R. Gadbail and V. Joshi, *World J. Surg. Oncol.*, 2013, **11**, 118.

33 F. Balkwill and A. Mantovani, *Lancet*, 2001, **357**, 539–545.

34 S. I. Grivennikov, F. R. Greten and M. Karin, *Cell*, 2010, **140**, 883–899.

35 L. Teng, G. Song, Y. Liu, X. Han, Z. Li, Y. Wang, S. Huan, X.-B. Zhang and W. Tan, *J. Am. Chem. Soc.*, 2019, **141**, 13572–13581.

36 Y. Zhou, X. Kuang, X. Yang, J. Li, X. Wei, W. J. Jang, S.-S. Zhang, M. Yan and J. Yoon, *Chem. Sci.*, 2024, **15**, 19669–19697.

37 B. Li, J. Tian, C. Wu, Z. Li, L. Qiao, Z. Xie, B. Song, Y. Shan, S. Chen, Y. Tang, Y. Ping and B. Liu, *Adv. Mater.*, 2024, **36**, 2405502.

38 T. C. Pham, V.-N. Nguyen, Y. Choi, S. Lee and J. Yoon, *Chem. Rev.*, 2021, **121**, 13454–13619.

39 S. Li, K. Gu, H. Wang, B. Xu, H. Li, X. Shi, Z. Huang and H. Liu, *J. Am. Chem. Soc.*, 2020, **142**, 5649–5656.

40 Y. Cai, Z. Wei, C. Song, C. Tang, W. Han and X. Dong, *Chem. Soc. Rev.*, 2019, **48**, 22–37.

41 Q. Jiang, J. Li, Z. Du, M. Li, L. Chen, X. Zhang, X. Tang, Y. Shen, D. Ma, W. Li, L. Li, N. Alifu, Q. Hu and J. Liu, *Adv. Healthcare Mater.*, 2024, 2400962.

42 M. Li, Y. Shao, J. H. Kim, Z. Pu, X. Zhao, H. Huang, T. Xiong, Y. Kang, G. Li, K. Shao, J. Fan, J. W. Foley, J. S. Kim and X. Peng, *J. Am. Chem. Soc.*, 2020, **142**, 5380–5388.

43 M. Li, J. Xia, R. Tian, J. Wang, J. Fan, J. Du, S. Long, X. Song, J. W. Foley and X. Peng, *J. Am. Chem. Soc.*, 2018, **140**, 14851–14859.

44 X. Ni, W. Shi, Y. Liu, L. Yin, Z. Guo, W. Zhou and Q. Fan, *Small*, 2022, **18**, 2200152.

45 Z. He, L. Zhao, Q. Zhang, M. Chang, C. Li, H. Zhang, Y. Lu and Y. Chen, *Adv. Funct. Mater.*, 2020, **30**, 1910301.

46 D. Cui, J. Huang, X. Zhen, J. Li, Y. Jiang and K. Pu, *Angew. Chem., Int. Ed.*, 2019, **58**, 5920–5924.

47 F. Lu, L. Li, M. Zhang, C. Yu, Y. Pan, F. Cheng, W. Hu, X. Lu, Q. Wang and Q. Fan, *Chem. Sci.*, 2024, **15**, 12086–12097.

48 Y. Dang, L. Ruan, Y. Tian, Z. Xu and W. Zhang, *Anal. Chem.*, 2021, **93**, 7625–7634.

49 P. Yuan, X. Xu, D. Hu, Y. Chen, J. Fan, S. Yao, Y. Piao, Z. Zhou, S. Shao, N. K. H. Slater, Y. Shen and J. Tang, *J. Am. Chem. Soc.*, 2023, **145**, 7941–7951.

50 F. Wang, S. Yu, Z. Xu, L. Li, Y. Dang, X. Xu, Y. Luo, Z. Cheng, H. Yu, W. Zhang, A. Zhang and C. Ding, *Anal. Chem.*, 2018, **90**, 7953–7962.